Bilateral interfaces in In_2Se_3-$CoIn_2$-$CoSe_2$ heterostructures boosting fast and robust sodium storage properties in MOF-derived hollow nanorods

Shuhao Xiao[a], Xinyan Li[a], Wensi Zhang[a], Yong Xiang[a], Tingshuai Li[a], Xiaobin Niu[a], Jun Song Chen[a], Qingyu Yan[b]**

S. Xiao, X. Li, W. Zhang, Prof. Y. Xiang, Prof. T. Li, Prof. X. Niu, Prof. J.S. Chen
[a]School of Materials and Energy, University of Electronic Science and Technology of China, Chengdu, 610054, China.
Email: jschen@uestc.edu.cn.

Prof. Q. Yan
School of Materials Science and Engineering, Nanyang Technological University, 50 Nanyang Avenue, Singapore 639798, Singapore.
Email: alexyan@ntu.edu.sg.

Abstract

Metal selenides are a group of promising candidates as the anode material for sodium-ion batteries due to their high theoretical capacity. However, the intrinsically low electrical and ionic conductivities as well as huge volume change during charge-discharge process give rise to an inferior sodium storage capability, which severely hinder their practical application. Herein, we have fabricated In_2Se_3/$CoSe_2$ hollow nanorods composed of In_2Se_3/$CoIn_2$/$CoSe_2$ by growing cobalt-based zeolitic imidazolate framework ZIF-67 on the surface of indium-based metal-organic framework MIL-68 followed by in-situ gaseous selenization. Because of the $CoIn_2$ alloy phase in between In_2Se_3 and $CoSe_2$, a heterostructure consisting of two alloy/selenide interfaces has been successfully constructed, offering synergistically enhanced electrical conductivity, Na diffusion process and structural stability, in comparison to the $CoIn_2$-free heterostructure with only two metal selenides. As expected, this unique construction delivers a high reversible capacity of 297.5 and 205.5 mAh g^{-1} at 5 and 10 A g^{-1} after 2000 cycles, respectively, and a superior rate performance of 371.6 mAh g^{-1} at even 20 A g^{-1}.

Keywords: metal selenide, heterostructure, multi-interface, anode material, sodium-ion battery

Introduction

With the fast development of portable electronic devices and electric vehicles, the demand for rechargeable batteries with high energy/powder densities and long cycle life is growing tremendously over the years[1]. Sodium-ion batteries (SIBs), which have a similar energy storage mechanism to lithium ion batteries (LIBs), are considered as a suitable replacement to LIBs due to the merits of rich natural resources, low cost and appropriate redox potential (-2.71 *vs* SHE) of Na[2]. However, the radius of Na atoms (~1.09 Å) is 55% larger than that of Li, which would cause sluggish diffusion kinetics and large volume change during the electrochemical processes, resulting in an inferior sodium storage capability, thus limiting the practical application of SIBs[3]. It is thus an urgent need to explore active materials to overcome the abovementioned shortcomings.

In the past decade, various anode materials have been extensively investigated for SIBs, such as carbonaceous materials[4], alloys[5], metal oxides[6] and dichalcogenides[7]. As promising anode materials for SIBs, metal selenides have received much attention considering their high theoretical capacity and volumetric capacity density[8]. In addition, owing to the large atom radius of selenium, the metal-selenium bonds are weaker than the metal-oxygen and metal-sulfur counterparts, leading to an improved efficiency of the conversion reaction in the selenides[9]. Take cobalt selenide ($CoSe_2$) as an example, it has stable chemical properties and environmental friendliness, thus has been reported as a promising anode material and extensively studied in SIBs[10]. However, like many other selenides, it still suffers from several drawbacks such as low intrinsic electronic conductivity, sluggish Na^+ diffusion kinetics and huge volume variation during Na^+ intercalation/extraction processes, leading to

inferior rate performance and poor cycling stability[11].

In order to boost the sodium storage abilities of metal selenides, many efforts have been devoted, such as composition hybridization[12], electrolyte modification[13] and nanostructure engineering[8b]. Recently, constructing heterostructures has shown to be an efficient strategy owing to the synergistic effect between the different components at the interface[14]. According to the previous studies, an internal electric field will be established in the heterostructure through a spontaneous electron migration across the interface[15]. This offers an extra driving force to accelerate the charge transfer, resulting in greatly enhanced electrical and ionic conductivities, thus giving rise to superior rate capability and cycle life of the electrode materials[16]. In addition, the active materials with heterostructures are often imbued with an improved structural stability compared to the phase-pure counterparts [17]. Because of these distinct advantages, constructing heterotructures with two different metal selenides have been employed to boost the electrochemical performance for SIBs [18]. For instance, the $SnSe_2$/ZnSe heterostructure delivered a remarkable electrochemical performance at high current densities due to its faster Na^+ diffusion rate than that of $SnSe_2$ and ZnSe[12]. These successful cases have proven that the construction of heterostructures with a single interface is beneficial to the electrochemical properties of the composite. However, in order to further uncover the potential of this unique category of materials, it is highly desirable to produce heterostructures with two or even multiple interfaces.

Herein, we fabricated metal-organic framework (MOF)-derived hollow nanorods consisting of heterostructured In_2Se_3-$CoIn_2$-$CoSe_2$ with two different interfaces. Rod-like indium-based MOF, MIL-68, was first synthesized as template for the subsequent coating of cobalt-based MOF, ZIF-67, giving rise to a MIL-68@ZIF-67 core-shell structure. Such a composite was then selenized under inert gas,

transforming the metal components into the corresponding selenides, accompanied by an inside-out hollowing process. By tuning the selenization temperature, the $CoIn_2$ alloy phase could be formed in addition to the metal selenides, giving rise to a heterostructure with In_2Se_3-$CoIn_2$ and $CoSe_2$-$CoIn_2$ bilateral interfaces. The theoretical calculation results revealed that such a unique heterostructure not only enhanced the adsorption and reduced the diffusion barrier of Na atoms, but also promoted spontaneous electron transfer across these interfaces, resulting in the improved electrical conductivity, Na ions diffusion process and structural stability of the as-prepared hollow nanorods. As expected, this tri-phase composite delivered a high reversible capacity of 297.5 and 205.5 mAh g^{-1} at 5 and 10 A g^{-1} after 2000 cycles, respectively, and a superior rate performance of 371.6 mAh g^{-1} at 20 A g^{-1}.

Results and Discussion

The overall fabrication procedure of the composite hollow nanorods is illustrated in Figure 1a. As both the starting template and indium source, MIL-68 (Figure 1b) with a hexagonal prism structure was first prepared, followed by the uniform deposition of ZIF-67 at room temperature (Figure 1c). It is interesting to observe that instead of the usual rhombic dodecahedral structure, the coated ZIF-67 showed as nanoparticles without a well-defined morphology, forming a densely packed outer layer which exhibited a corn-like morphology. This could be probably attributed to the high affinity between these two MOFs, giving rise to a fast yet uniform nucleation of ZIF-67 on MIL-68. After carbonization, the particles on the surface of hexagonal prism condensed into nanoflakes (Figure 1d). The final product was obtained via a gas-phase selenization under the flow of Ar/H_2, while the hexagonal prism nanostructure could be largely retained (Figure 1e). As expected, $In_2Se_3/CoSe_2$-400 demonstrated an almost identical morphology as $In_2Se_3/CoSe_2$-450 (Figure S1), while In_2Se_3 exhibited severe structural

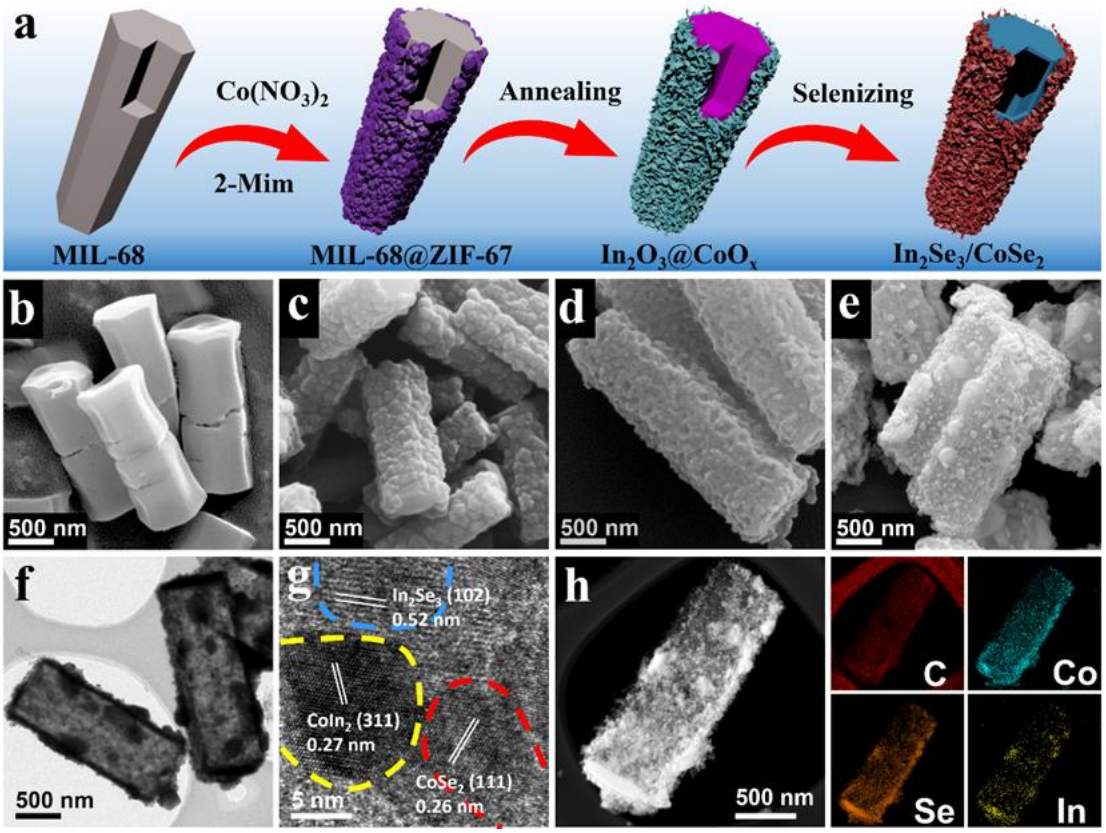

Figure 1. (a) Schematic illustration of the synthetic process. SEM images of (b) In-MOF, (c) In-MOF@ZIF-67, (d) In_2O_3@CoO_x, (e) In_2Se_3/$CoSe_2$-450; (f) TEM image, (g) HRTEM image, and (f) HAADF-STEM image and corresponding elemental mapping of In_2Se_3/$CoSe_2$-450.

collapse, which could be probably due to the absence of the outer ZIF-67 protective layer. The internal structure of as-prepared In_2Se_3/$CoSe_2$-450 is elucidated by transmission electron microscopy (TEM), and a well-defined inner cavity can be clearly observed (Figure 1f). The generation of the hollow structure could possibly be attributed to the Kirkendall effect[19], which has been reported in other types of MOF-derived materials[20]. Specifically, during the selenization process which initiated at the surface of the MOFs, selenium atoms diffused from the surface to the interior of the nanorods while indium atoms flows outward at a different rate[21]. The discrepant diffusion rates of the two kinds of atoms would be balanced by the movement of voids, thus giving rise to the hollow interior and a thin shell with a thickness of less than 100 nm. As displayed in the high-resolution TEM (HRTEM) result

of $In_2Se_3/CoSe_2$-450 (Figure 1g), three different sets of lattice fringes are clearly visible. The interplanar spacings of 0.52 and 0.26 nm were identified, corresponding to the (102) plane of hexagonal In_2Se_3 (JCPDS: 71-0250) and (111) plane of orthorhombic $CoSe_2$ (JCPDS: 53-0449), respectively. At the same time, the third lattice fringes with a spacing of 0.27 nm corresponds to the (311) plane of orthorhombic $CoIn_2$ (JCPDS: 71-0329). These three different phases contributed to a heterostructure with two interfaces which were marked by dashed line with different colors. Even though $In_2Se_3/CoSe_2$-400 (Figure S2) exhibited the same hollow structure as $In_2Se_3/CoSe_2$-450, only two selenide phases were observed under HRTEM, corresponding to a single interface of In_2Se_3-$CoSe_2$. Meanwhile, the uniform distributions of C, In, Co and Se elements of an individual $In_2Se_3/CoSe_2$-450 hollow nanorod were confirmed by element mapping (Figure 1h), suggesting the formation of a homogeneous solid solution of In_2Se_3, $CoSe_2$ and $CoIn_2$.

Such a three-phase composition was further verified by X-ray diffraction (XRD). As depicted in Figure S3, such a selenization method was proven to be quite effective that all the precursor samples were completely converted into the corresponding selenides even at a relatively low temperature of 400 ^oC, with no presence of peaks due to the parental or impurity phases. Moreover, when the temperature was increased to 450 ^oC, most of the identified peaks of $In_2Se_3/CoSe_2$-450 could be attributed to hexagonal In_2Se_3 (JCPDS: 71-0250) and orthorhombic $CoSe_2$ (JCPDS: 53-0449). Additional sharp peaks which located at 31.7^o and 33.6^o could be ascribed to orthorhombic $CoIn_2$ (JCPDS: 71-0329).

Quantitative analysis by inductively coupled plasma-atomic emission spectrometry (ICP-AES) suggested that the atomic ratio of In and Co in $In_2Se_3/CoSe_2$-450 was 1: 0.56. Subsequently, the weight content of carbon in this sample was measured via thermogravimetric (TG) analysis in air (Figure S3d).

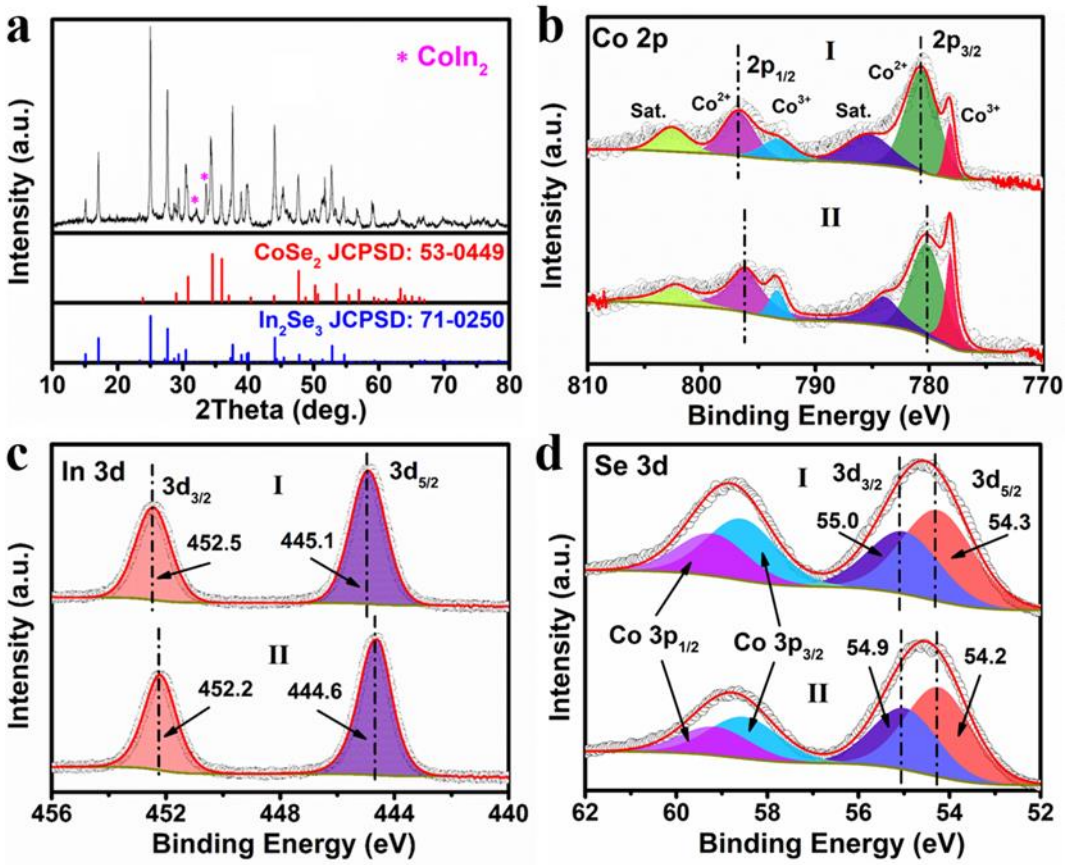

Figure 2. (a) XRD pattern of $In_2Se_3/CoSe_2$-450. High-resolution XPS spectra of (b) Co 2p, (c) In 3d and (d) Se 3d of various samples: (I) $In_2Se_3/CoSe_2$-450 and (II) $In_2Se_3/CoSe_2$-400.

The main weight loss from 340 to 550 °C can be ascribed to the volatilization of SeO_2 and the combustion of carbon. After that, the final residue with a mass content of 42.9 wt% at 800 °C could be attributed to the oxide phases of In_2O_3 and Co_3O_4. In tandem with the ICP-AES results, the mass content of In_2Se_3 and $CoSe_2$ in $In_2Se_3/CoSe_2$-450 could be calculated to be 62.7 and 28.2 wt%, respectively. Therefore, the weight percentage of carbon in the composite was computed to be 9.1%. The surface structures of $In_2Se_3/CoSe_2$-450 and $In_2Se_3/CoSe_2$-400 were further analyzed by the Brunauer−Emmett−Teller (BET) method. The N_2 adsorption and desorption isotherms of the as-prepared samples (Figure S4) belong to typical IV adsorption isotherm with a type H3 hysteresis loop, suggesting the presence of mesopores in the hollow nanorods. Moreover, $In_2Se_3/CoSe_2$-450 possesses

a specific surface area and a total pore volume of 88.3 m^2 g^{-1} and 0.066 cm^3 g^{-1}, respectively, which are higher than those of $In_2Se_3/CoSe_2$-400 (48.6 m^2 g^{-1} and 0.051 cm^3 g^{-1}). As shown in the inset in Figure S4, $In_2Se_3/CoSe_2$-450 and $In_2Se_3/CoSe_2$-400 exhibited pore size distributions generally in the range of 2-25 nm, and average pore sizes at about 1.5 and 2.1 nm, respectively.

In addition, the valence and chemical states of $In_2Se_3/CoSe_2$-450 and $In_2Se_3/CoSe_2$-400 were determined by X-ray photoelectron spectroscopy (XPS). In the Co 2p spectrum of $In_2Se_3/CoSe_2$-450 (Figure 2b), the strong peaks located at 769.9 and 780.7 eV can be ascribed to Co $2p_{3/2}$ and $2p_{1/2}$ of the Co^{2+} state, respectively, which belong to the $CoSe_2$ phase. Meanwhile, the peaks centered at 793.4 and 778.3 eV are characteristics of the Co^{3+} state. The existence of Co^{3+} could be attributed to the partial oxidation on the $CoSe_2$ surface in air[10c]. Moreover, the In 3d spectrum (Figure 2c) can be deconvoluted into two peaks at 445.0 and 452.5 eV, corresponding to In $3d_{5/2}$ and $3d_{3/2}$, respectively[22]. Notably, compared to $In_2Se_3/CoSe_2$-400, the peaks in the Co 2p and In 3d spectra of $In_2Se_3/CoSe_2$-450 shifted to higher binding energies, revealing an enhanced electronic coupling between the elements[12], which could be due to the formed $CoIn_2$ alloy phase. Furthermore, as shown in Figure 2d, the Se 3d spectrum clearly exhibited two peaks located at 54.2 and 55.4 eV, corresponding to Se $3d_{5/2}$ and $3d_{3/2}$, respectively[23]. The additional peaks centered at 58.6 and 59.2 eV could be assigned to Co $3p_{3/2}$ and $3p_{1/2}$, respectively, which is consistent with previous report about $CoSe_2$[11a].

The electrochemical performances of $In_2Se_3/CoSe_2$-450, $In_2Se_3/CoSe_2$-400, pure In_2Se_3 and $CoSe_2$ were investigated in a coin-type 2032 cell using sodium metal as the counter electrode. The cyclic voltammetry (CV) of these four samples was measured with a voltage window of 0.01-2.5 V at 0.1 mV s^{-1} (Figure 3a, S5). Noticeably, the peaks in the CVs of $In_2Se_3/CoSe_2$-450 and $In_2Se_3/CoSe_2$-400 are comparable, indicating similar electrochemical reactions and the inactive nature of $CoIn_2$ in

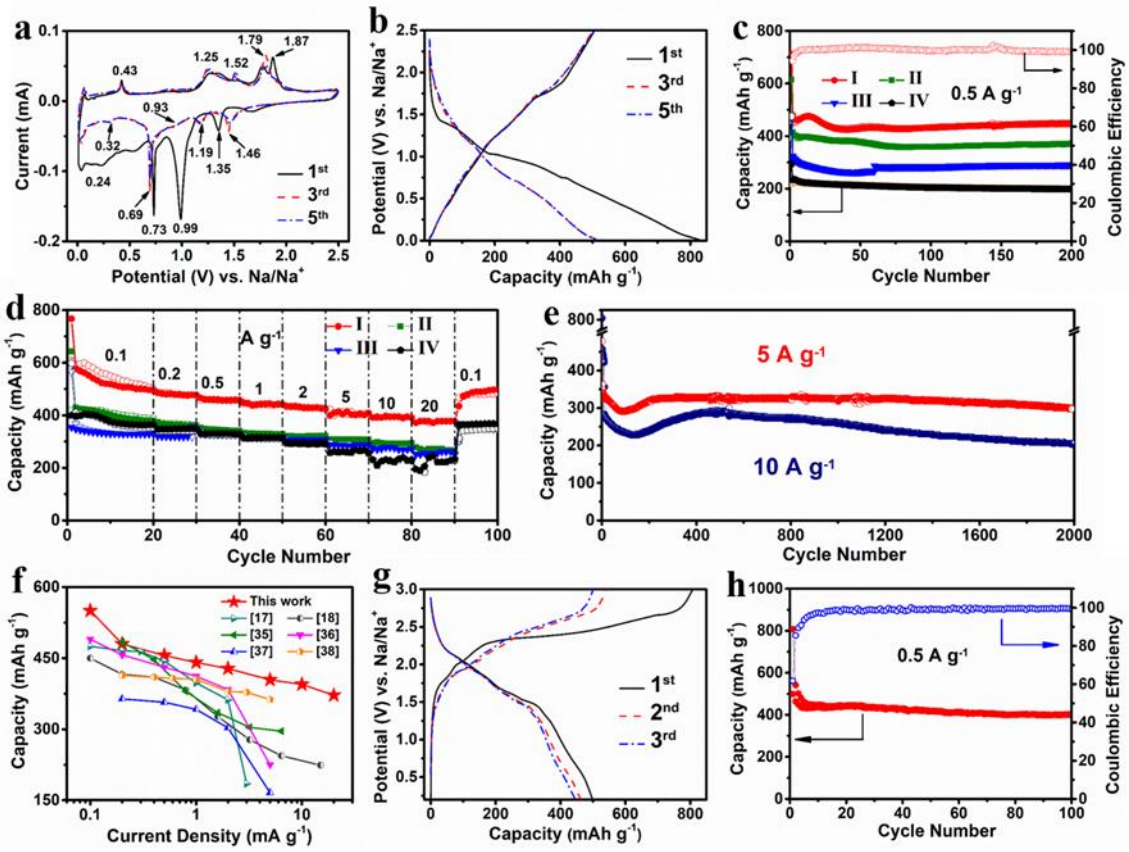

Figure 3. Electrochemical performance of SIB. (a) CV profiles of $In_2Se_3/CoSe_2$-450 at a scan rate of 0.1 mV s^{-1}. (b) Discharge/charge curves of $In_2Se_3/CoSe_2$-450 at 0.1 A g^{-1}. (c) Cycling performance at 0.5 A g^{-1} and (d) rate capability of (I) $In_2Se_3/CoSe_2$-450, (II) $In_2Se_3/CoSe_2$-400, (III) In_2Se_3 and (IV) $CoSe_2$. (e) Long-term cyclability of the $In_2Se_3/CoSe_2$-450 anode. (f) Comparison of rate performances between $In_2Se_3/CoSe_2$-450 and other selenide-based SIB anodes. (g) Discharge/charge curves and (h) cycling performance of a $In_2Se_3/CoSe_2$-450//$Na_3V_2(PO_4)_3$ full-cell at 0.5 A g^{-1}.

sodium storage. As discussed in previous works, the main reactions of Na^+ storage in $CoSe_2$ during the discharge-charge cycles are as follow[24]:

Discharging:

$$CoSe_2 + xNa + xe^- \rightarrow Na_xCoSe_2 \quad (1)$$

$$Na_xCoSe_2 + (2-x)Na^+ + (2-x)e^- \rightarrow CoSe + Na_2Se \quad (2)$$

$$CoSe + 2Na^+ + 2e^- \rightarrow Co + Na_2Se \quad (3)$$

Charging:

$$Co + 2Na_2Se \rightarrow Na_xCoSe_2 + (4-x)Na^+ + (4-x)e^- \quad (4)$$

$$Na_xCoSe_2 \rightarrow CoSe_2 + xNa^+ + xe^- \quad (5)$$

The Na^+ storage mechanism of In_2Se_3 is analogous to that of In_2S_3 due to the similar electrochemical properties of S and Se[14b]. Therefore, the electrochemical process of In_2Se_3 consists of intercalation, conversion and alloying/dealloying reactions, as shown below:

$$In_2Se_3 + xNa + xe^- \rightarrow Na_xIn_2Se_3 \quad (6)$$

$$Na_xIn_2Se_3 + (6-x)Na^+ + (6-x)e^- \rightarrow 2In + 3Na_2Se \quad (7)$$

$$In + Na^+ + e^- \rightarrow NaIn \quad (8)$$

As shown in Figure 3a, the CV curve of $In_2Se_3/CoSe_2$-450 in the first cycle displays two reduction peaks at 1.35 and 0.99 V, which disappear in the subsequent scans and thus possibly correspond to the irreversible intercalation of Na^+ and the formation of solid electrolyte interphase (SEI)[24]. A sharp peak located at 0.73 V is correlated to the conversion reaction of CoSe and In_2Se_3 (Equation (3) and (7)) and the peak displayed at 0.24 V can be attributed to the alloying reaction of In to give Na_xIn (Equation (8))[14b]. In the following anodic scan, the peaks at 0.43, 1.25 and 1.52 V are associated with the dealloying process and formation of In_2Se_3. Two adjacent peaks appearing at 1.79 and 1.87 V correspond to the desodiation process of $CoSe_2$ (Equation (4) and (5))[10c]. Moreover, the 3rd and 5th cycles exhibit well-overlapped CV curves, indicating the high reversibility of these electrochemical reactions. In addition, two new reduction peaks appeared at 1.46 and 1.19 V, which could be attributed to the reaction (Equation (1) and (2)) during discharge[24]. The slight shifts of the peaks in the following cycles could be probably ascribed to the structural reorganization during repeated Na insertion/deinsertion process.

The galvanostatic discharge/charge curves of the 1st, 3rd and 5th cycles of $In_2Se_3/CoSe_2$-450 at a current density of 0.1 A g^{-1} was shown in Figure 3b, and the voltage plateaus match well with the CV results. The discharge and charge capacities of the first cycle are as high as 827.5 and 506.2 mAh g^{-1}, respectively, with an initial Coulombic efficiency of 61.2%, and the charge/discharge curves of the 3rd and 5th cycles display no observable difference. The cycling performances of as-prepared samples are compared in Figure 3c, where all of them show quite stable capacities. $In_2Se_3/CoSe_2$-450 delivers the highest reversible capacity of 445.0 mAh g^{-1} after 200 cycles at 0.5 A g^{-1}, with a capacity retention ratio of 95.7%. The slight but noticeable increase in capacity during the first 20 cycles can be related to the activation process of active materials[14a, 25]. Apparently, $In_2Se_3/CoSe_2$-400 show a capacity of 370.2 mAh g^{-1} after 200 cycles, which is lower than that of $In_2Se_3/CoSe_2$-450 but higher than pure In_2Se_3 (290.6 mAh g^{-1}) and $CoSe_2$ (197.3 mAh g^{-1}). Post-mortem SEM measurement was carried out to confirm the integrity of the structure (Figure S6). Evidently, the rod-like structure of $In_2Se_3/CoSe_2$-450 could be well maintained with no severe structural collapse after the long-term test, indicating a superior structural stability.

The rate performance of these samples was also analyzed at different current rates from 0.1 to 20 A g^{-1} (Figure 3d). It is apparent that the $In_2Se_3/CoSe_2$-450 delivers the highest reversible capacities at these current rates among the four samples, and even at the highest current of 20 A g^{-1}, a stable capacity of 372 mAh g^{-1} could be achieved, suggesting an enhanced high-rate performance. In addition, the capacity quickly recovered to 498.3 mAh g^{-1} when the current density dropped to 0.1 A g^{-1}. The corresponding charge/discharge curves demonstrated well-defined voltage platforms with no significant distortion at various rates (Figure S7), suggesting a low electrochemical polarization. The long-term cycling stability of $In_2Se_3/CoSe_2$-450 was further analyzed at high current densities (Figure

3e), and reversible capacities of 297.5 and 205.5 mAh g^{-1} can still be delivered even after 2000 cycles at 5 and 10 A g^{-1}, respectively. The capacity retention is calculated to be 90.0% at 5 A g^{-1}, corresponding to a low capacity decay of only 0.005 % per cycle. The comparison of rate performance between $In_2Se_3/CoSe_2$-450 and other reported metal selenides-based electrodes is presented in Figure 3f[10b, 10c, 26] and Table S1, showing the advantageous Na^+ storage properties of our sample, especially at higher current densities.

Inspired by the remarkable electrochemical performance of the half-cell, we also accessed the potential of $In_2Se_3/CoSe_2$-450 for practical application by evaluating the full-cell performance using $Na_3V_2(PO_4)_3$ (NVP) as the cathode. The cycling performance of the NVP cathode was first investigated (Figure S8), displaying a reversible capacity of about 92.5 mAh g^{-1} after 100 cycles at 0.5 C (1C = 117 mA g^{-1}). The typical galvanostatic discharge and charge curves of the full cell cycled between 0.2 and 3.0 V at 0.5 A g^{-1} are displayed in Figure 3g, where a high initial discharge capacity of about 498.9 mAh g^{-1} can be obtained. Remarkably, the full cell displays a quite stable cyclability after a rapid decay in the first 5 cycles and a high reversible capacity of 402.7 mAh g^{-1} after 100 cycles at 0.5 A g^{-1}, indicating the promising potential for practical SIB application.

In order to further investigate the electrochemical kinetics of the as-prepared electrodes, the capacity contribution was studied in-depth by the CV analysis at various scan rates from 0.2 to 5 mV s^{-1} (Figure 4a). $In_2Se_3/CoSe_2$-450 shows CV curves of similar shapes with only minor peak shifts as the scan rate increases. The relationship between current (i) and scan rate (v) can be described using equation[27]:

$$i = av^b \qquad (9)$$

$$\log i = b \log v + \log a \qquad (10)$$

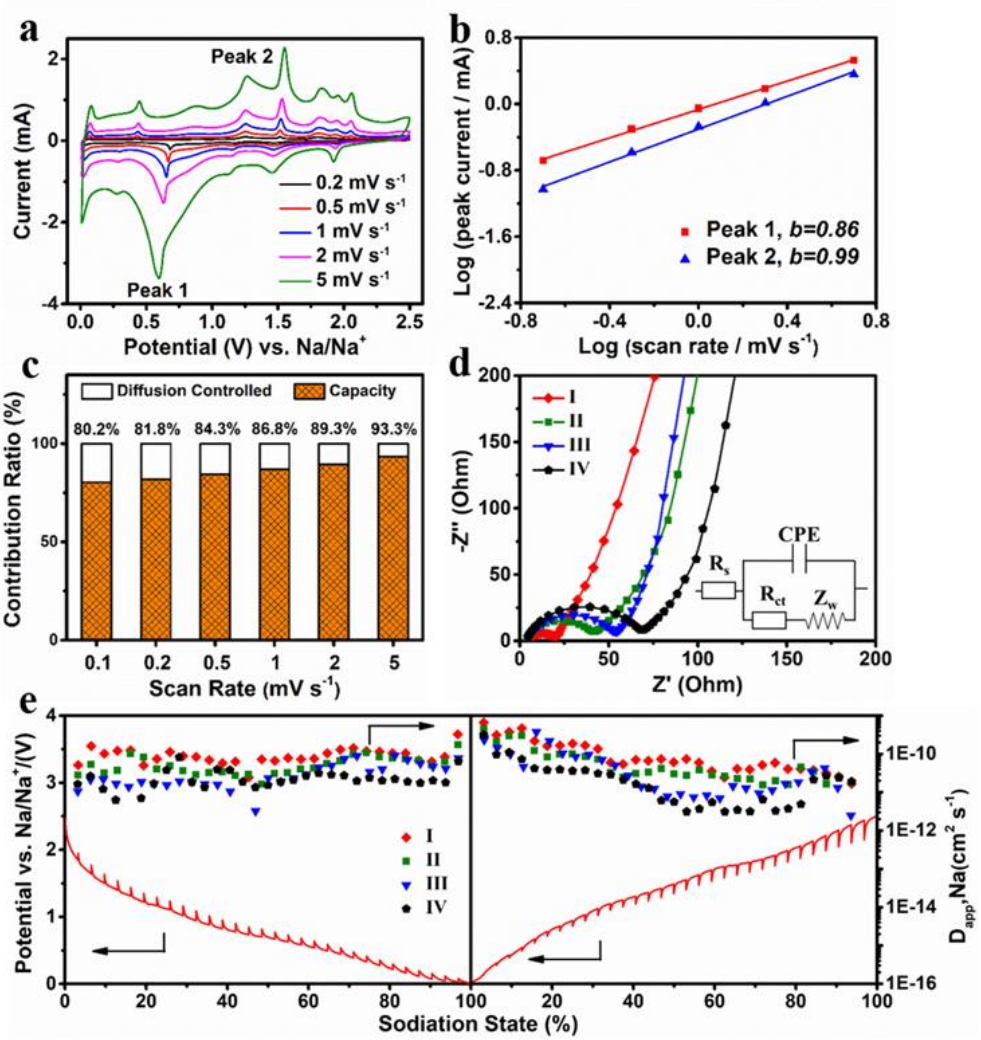

Figure 4. (a) CV curves at various scan rates, (b) corresponding log i versus log v plot at each redox peak and (c) normalized ratio of diffusion-controlled or capacitive contributions at various scan rates. (d) Nyquist plots and (e) GITT curves and the corresponding Na^+ diffusion coefficients for (I) $In_2Se_3/CoSe_2$-450, (II) $In_2Se_3/CoSe_2$-400, (III) In_2Se_3 and (IV) $CoSe_2$.

where a and b are adjustable parameters and the b value represents the charge storage behavior[28], and the range of which is typically between 0.5 and 1.0. When the electrochemical process is mainly controlled by ionic diffusion, b is close to 0.5; when the b value approaches 1, the process is dominated by capacitive effect. The b values of the two peaks marked in Figure 4a were calculated to be 0.86 and 0.99 (Figure 3b), suggesting that the Na^+ storage process of $In_2Se_3/CoSe_2$-450 was predominantly

controlled by capacitive process. Meanwhile, $In_2Se_3/CoSe_2$-400, pure In_2Se_3 and $CoSe_2$ all showed relatively low b values (Figure S9), indicating that the Na^+ storage process in these samples contained both diffusion and capacitive process. In addition, the contribution of capacitive effect can be quantified using equation[29]:

$$i = k_1 v + k_2 v^{0.5} \qquad (11)$$

where k_1v and $k_2v^{0.5}$ represent the capacity and diffusion contributions, respectively. Accordingly, the capacitive contribution of $In_2Se_3/CoSe_2$-450 is calculated to be 80.2% at 0.1 mV s^{-1} and increases to 93.3% at 5 mV s^{-1}, with a quantitative analysis (Figure S10) that is analogous to other transition metal selenides.

To further investigate the dynamic process of the as-prepared samples during Na^+ diffusion, the electrochemical impedance spectroscopy (EIS) measurements were conducted. As depicted in Figure 4d, the Nyquist plots of the four samples show similar profiles, which consist of a depressed semi-circle in the high-frequency region, which corresponds to the charge transfer resistance (R_{ct}), and an up-sloping line in the low-frequency region representing the Warburg diffusion process (Z_w)[30]. The R_{ct} of $In_2Se_3/CoSe_2$-450 is calculated to be 15.7 Ω (Table S2), which is much lower than $In_2Se_3/CoSe_2$-400 (38.0 Ω), pure In_2Se_3 (51.9 Ω) and $CoSe_2$ (67.3 Ω), implying the fastest charge transfer process in $In_2Se_3/CoSe_2$-450. Meanwhile, the diffusion coefficients of Na^+ in our electrodes were measured by the Galvanostatic Intermittent Titration Technique (GITT), and could be calculated based on a simplified equation[31]:

$$D = \frac{4L^2}{\pi\tau}\left(\frac{\Delta E_s}{\Delta E_t}\right)^2$$

where ΔE_s is the potential change (V) due to the current pulse, ΔE_t stands for the potential change (V) during the galvanostatic discharge after eliminating the i_R drop, L is the Na^+ diffusion length, which

could be simply taken as the thickness of the electrode and τ represents the relaxation time (s). The GITT curves and the corresponding D values of the discharge and charge processes are shown in Figure 4e. The diffusion coefficients of Na^+ ($D_{app.Na}$) of the four samples exhibit a similar variation trend, and the $In_2Se_3/CoSe_2$-450 electrode show the highest $D_{app.Na}$ in the range between 1×10^{-11} and 1×10^{-10} cm^2 s^{-1}. Consistent with the above EIS analysis, these GITT results further revealed the fact that building In_2Se_3-$CoIn_2$-$CoSe_2$ heterostructure with two interfaces can effectively reduce the charge transfer resistance, accelerate the Na^+ migration and thus result in a superior rate performance.

To reveal the exact role of In_2Se_3-$CoIn_2$-$CoSe_2$ heterostructure in improving the Na^+ storage properties, density functional theory (DFT) calculation was employed to investigate the effects of the different interfaces. According to the TEM and XRD measurement, we constructed three different heterostructure models, where $In_2Se_3/CoSe_2$-400 consisted only one interface of In_2Se_3-$CoSe_2$, while the bilateral interfaces of In_2Se_3-$CoIn_2$ and $CoSe_2$-$CoIn_2$ are present in $In_2Se_3/CoSe_2$-450. Figure 5a displays the migration paths of Na at these three different interfaces. The Na diffusion energy barrier of In_2Se_3-$CoSe_2$ is 1.37 eV (Figure 5b), which is apparently higher than that of In_2Se_3-$CoIn_2$ (0.76 eV) and $CoSe_2$-$CoIn_2$ (0.57 eV), revealing a faster Na diffusion process in In_2Se_3-$CoIn_2$ and $CoSe_2$-$CoIn_2$. Additionally, the adsorption energies of Na atom (Figure 5c) on In_2Se_3-$CoIn_2$ (-2.66 eV) and $CoSe_2$-$CoIn_2$ (-1.56 eV) are higher than on $In_2Se_3/CoSe_2$ (-1.44 eV), suggesting more stable adsorption in the formers, which is mainly due to the presence of the $CoIn_2$ phase[32].

Meanwhile, in the calculated density of states (DOS) of these models (Figure 5d), In_2Se_3-$CoSe_2$ possesses a significant band gap (0.3 eV), while In_2Se_3-$CoIn_2$ and $CoSe_2$-$CoIn_2$ exhibit no band gaps and an enhanced electron density near the Fermi level[33]. Considering that this phenomenon might be caused by the electron transfer between different phases, the work functions (E_w) of In_2Se_3, $CoIn_2$ and

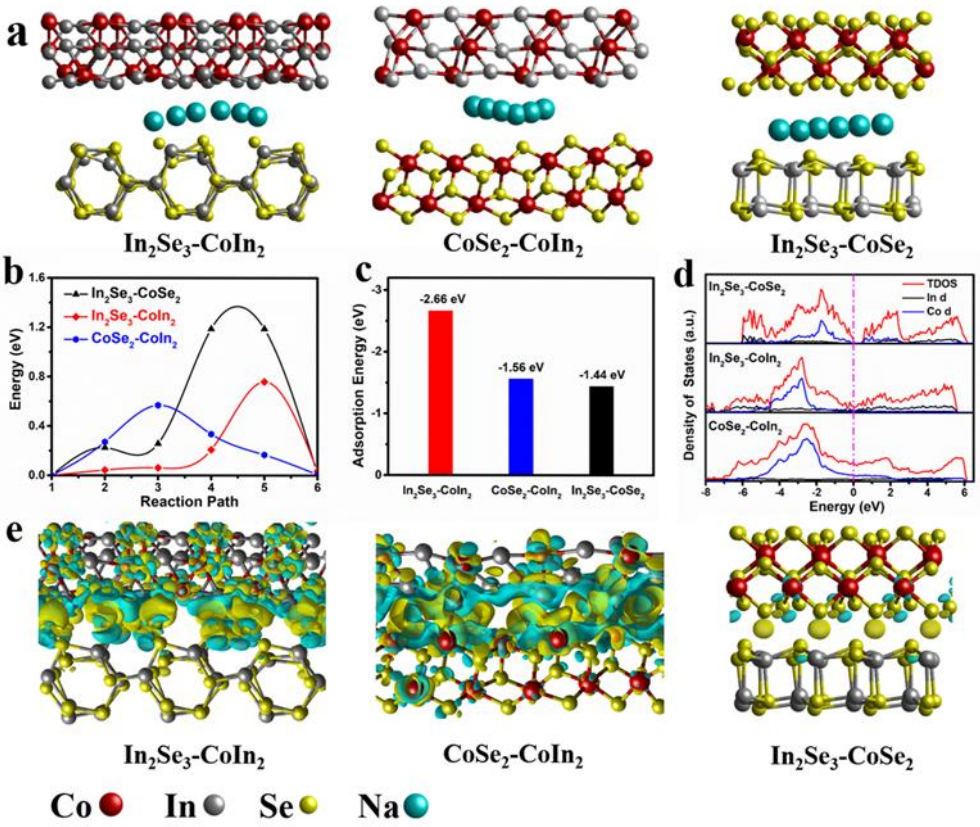

Figure 5. (a) Na migration paths and (b) corresponding energy barriers in the In_2Se_3-$CoIn_2$, $CoSe_2$-$CoIn_2$ and the In_2Se_3-$CoSe_2$ heterostructured interfaces. (c) Na adsorption energies, (d) calculated DOS and (e) charge density difference of the three different models. The yellow and blue clouds represent the negative and positive charge differences, respectively.

$CoSe_2$ were calculated and the corresponding energy distribution curves are presented in Figure S11. The E_w can be derived by the following equation[34]:

$$E_w = E_{vac} - E_f$$

where E_{vac} and E_f represent the vacuum layer level and Fermi level, respectively, which are marked as dashed platforms in the figures. The $CoIn_2$ exerts a higher E_w (6.34 eV) than In_2Se_3 (5.51 eV) and $CoSe_2$ (5.24 eV), indicating that the free electrons could flow from $CoIn_2$ to In_2Se_3 and $CoSe_2$ at the In_2Se_3-$CoIn_2$ and $CoSe_2$-$CoIn_2$ interfaces[35]. This would promote the establishment of internal electric fields in these heterostructures, thus reducing the electrical conductivity and accelerating Na^+

migration during the cycling process[36]. In contrast, the difference of the E_w values in In_2Se_3 and $CoSe_2$ is very trivial, implying a low charge transfer efficiency between these two phases. Such a strong tendency in charge redistribution is further illustrated by the charge density differences of these models (Figure 5e), where more significant charge accumulation/depletion could be clearly observed at the interfaces of In_2Se_3-$CoIn_2$ and $CoSe_2$-$CoIn_2$ than In_2Se_3-$CoSe_2$.

Conclusion

In summary, In_2Se_3-$CoIn_2$-$CoSe_2$ heterostructure with In_2Se_3-$CoIn_2$ and $CoSe_2$-$CoIn_2$ bilateral interfaces was successfully constructed in MOF-derived hollow nanorods. The $CoIn_2$ alloy phase could be introduced into the composite by tuning the selenization temperature, leading to a strong coupling between the In and Co atoms. The DFT results suggested that $CoIn_2$ could not only enhance the adsorption and reduce the diffusion barrier of Na atoms, but also optimize the electronic structure via spontaneous electron transfer, resulting in a smaller charge transfer resistance and faster Na^+ migration at the In_2Se_3-$CoIn_2$ and $CoSe_2$-$CoIn_2$ interfaces than the $CoIn_2$-free In_2Se_3-$CoSe_2$ counterpart. As a result, the sample with the bilateral interface demonstrated extraordinary sodium storage capabilities with 297.5 and 205.5 mAh g^{-1} at 5 and 10 A g^{-1} after 2000 cycles, respectively, and excellent rate performance of 371.6 mAh g^{-1} at 20 A g^{-1}. Such sodium storage properties are significantly better than the sample with the single In_2Se_3-$CoSe_2$ interface, phase-pure In_2Se_3 and $CoSe_2$, and also other selenide-based anodes. Our work presented an innovative strategy to construct advanced heterostructures with multiple interfaces, which can be applied for the design of high-performance materials for electrochemical storage systems.

References

[1] a) S. Chu, A. Majumdar, *Nature* **2012**, 488, 294; b) K. J. Griffith, K. M. Wiaderek, G. Cibin, L. E. Marbella, C. P. Grey, *Nature* **2018**, 559, 556.

[2] B. Dunn, H. Kamath, J.-M. Tarascon, *Science* **2011**, 334, 928.

[3] P. K. Nayak, L. Yang, W. Brehm, P. Adelhelm, *Angew. Chem. Int. Ed. Engl.* **2018**, 57, 102.

[4] a) Y. Wen, K. He, Y. Zhu, F. Han, Y. Xu, I. Matsuda, Y. Ishii, J. Cumings, C. Wang, *Nat. Commun* **2014**, 5, 4033; b) N. Sun, Z. Guan, Y. Liu, Y. Cao, Q. Zhu, H. Liu, Z. Wang, P. Zhang, B. Xu, *Adv. Energy Mater.* **2019**, 9, 1901351.

[5] a) W. Li, S. Hu, X. Luo, Z. Li, X. Sun, M. Li, F. Liu, Y. Yu, *Adv. Mater.* **2017**, 29, 1605820; b) J. Sun, H. W. Lee, M. Pasta, H. Yuan, G. Zheng, Y. Sun, Y. Li, Y. Cui, *Nat. Nanotech.* **2015**, 10, 980.

[6] a) Q. Deng, F. Chen, S. Liu, A. Bayaguud, Y. Feng, Z. Zhang, Y. Fu, Y. Yu, C. Zhu, *Adv. Funct. Mater.* **2020**, 30, 1908665; b) H. B. Kong, Y. S. Wu, W. Z. Hong, C. S. Yan, Y. Y. Zhao, G. Chen, *Energy Storage Mater.* **2020**, 24, 610.

[7] a) Y. Fang, D. Luan, Y. Chen, S. Gao, X. W. D. Lou, *Angew. Chem. Int. Ed.* **2020**, 59, 7178; b) Y. Huang, X. Hu, J. Li, J. Zhang, D. Cai, B. Sa, H. Zhan, Z. Wen, *Energy Storage Mater.* **2020**, 29, 121.

[8] a) S. Xiao, Z. Li, J. Liu, Y. Song, T. Li, Y. Xiang, J. S. Chen, Q. Yan, *Small* **2020**, 16, 2002486; b) Y. Fang, X. Y. Yu, X. W. Lou, *Angew. Chem.* **2018**, 130, 10007.

[9] M. Luo, H. Yu, F. Hu, T. Liu, X. Cheng, R. Zheng, Y. Bai, M. Shui, J. Shu, *Chem. Eng. J.* **2020**, 380, 122557.

[10] a) K. Zhang, M. H. Park, L. M. Zhou, G. H. Lee, W. J. Li, Y. M. Kang, J. Chen, *Adv. Funct. Mater.* **2016**, 26, 6728; b) Y. Fang, X.-Y. Yu, X. W. D. Lou, *Adv. Mater.* **2018**, 30, 1706668; c) H. Yin, H.-Q. Qu, Z. Liu, R.-Z. Jiang, C. Li, M.-Q. Zhu, *Nano Energy* **2019**, 58, 715.

[11] a) B. Zhao, Q. Liu, G. Wei, J. Wang, X.-Y. Yu, X. Li, H. B. Wu, *Chem. Eng. J.* **2019**, 378, 122206; b) S. H. Yang, S.-K. Park, Y. C. Kang, *Chem. Eng. J.* **2019**, 370, 1008.

[12] P. Liu, J. Han, K. Zhu, Z. Dong, L. Jiao, *Adv. Energy Mater.* **2020**, 10, 2000741.

[13] S. Y. Lu, T. X. Zhu, H. Wu, Y. K. Wang, J. Li, A. Abdelkaderkh, K. Xi, W. Wang, Y. G. Li, S. J. Ding, G. X. Gao, R. V. Kumarh, *Nano Energy* **2019**, 59, 762.

[14] a) L. Cao, X. Gao, B. Zhang, X. Ou, J. Zhang, W.-B. Luo, *ACS Nano* **2020**, 14, 3610; b) Y. Huang, Z. Wang, Y. Jiang, S. Li, M. Wang, Y. Ye, F. Wu, M. Xie, L. Li, R. Chen, *Adv. Sci* **2018**, 5, 1800613.

[15] C. Z. Zhang, F. Han, F. Wang, Q. D. Liu, D. W. Zhou, F. Q. Zhang, S. H. Xu, C. L. Fan, X. K. Li, J. S. Liu, *Energy Storage Mater.* **2020**, 24, 208.

[16] S. Xiao, X. Li, T. S. Li, Y. Xiang, J. S. Chen, *J. Mater. Chem. A* **2021**, DOI: 10.1039/d0ta12417f.

[17] G. Chen, L. Yan, H. Luo, S. Guo, *Adv. Mater.* **2016**, 28, 7580.

[18] a) G. Fang, Q. Wang, J. Zhou, Y. Lei, Z. Chen, Z. Wang, A. Pan, S. Liang, *ACS Nano* **2019**, 13, 5635; b) J. Yuan, W. Liu, X. Zhang, Y. Zhang, W. Yang, W. Lai, X. Li, J. Zhang, X. Li, *J. Power Sources* **2020**, 455, 227937.

[19] Y. Yin, R. M. Rioux, C. K. Erdonmez, S. Hughes, G. A. Somorjai, A. P. Alivisatos, *Science* **2004**, 304, 711.

[20] H. Hu, J. Zhang, B. Guan, X. W. Lou, *Angew. Chem. Int. Ed.* **2016**, 55, 9514.

[21] S. Dong, C. Li, Z. Li, L. Zhang, L. Yin, *Small* **2018**, 14, 1704517.

[22] X. Wang, J.-Y. Hwang, S.-T. Myung, J. Hassoun, Y.-K. Sun, *ACS Appl. Mater. Inter.* **2017**, 9, 23723.

[23] X. C. Ren, J. S. Wang, D. M. Zhu, Q. W. Li, W. F. Tian, L. Wang, J. B. Zhang, L. Miao, P. K. Chu, K. F. Huo, *Nano Energy* **2018**, 54, 322.

[24] Y. Tang, Z. Zhao, X. Hao, Y. Wang, Y. Liu, Y. Hou, Q. Yang, X. Wang, J. Qiu, *J. Mater. Chem. A* **2017**, 5, 13591.

[25] a) F. Zhang, Y. Shen, M. Shao, Y. Zhang, B. Zheng, J. Wu, W. Zhang, A. Zhu, F. Huo, S. Li, *ACS Appl. Mater. Inter.* **2019**, 12, 2346; b) J. Liu, S. Xiao, X. Li, Z. Li, X. Li, W. Zhang, Y. Xiang, X. Niu, J. S. Chen, *Chem. Eng. J.* **2021**, 417, 129279.

[26] a) P. Ge, H. Hou, S. Li, L. Huang, X. Ji, *ACS Appl. Mater. Inter.* **2018**, 10, 14716; b) X. Yang, S. Wang, D. Y. W. Yu, A.

L. Rogach, *Nano Energy* **2019**, 58, 392; c) E. C. Atangana, H. Huang, H. Hong, G. Liu, L. Zhang, *Energy Storage Mater.* **2020**, 24, 167; d) T. Liu, S. Hou, Y. Li, Y. Guo, C. Yang, L. Zhao, *ACS Appl. Energ. Mater.* **2020**, 3, 9558.

[27] J. Wang, J. Polleux, J. Lim, B. Dunn, *J. Phys. Chem. C* **2007**, 111, 14925.

[28] X. Xu, R. Zhao, W. Ai, B. Chen, H. Du, L. Wu, H. Zhang, W. Huang, T. Yu, *Adv. Mater.* **2018**, 30, 1800658.

[29] C. Lv, H. Liu, D. Li, S. Chen, H. Zhang, X. She, X. Guo, D. Yang, *Carbon* **2019**, 143, 106.

[30] a) J. Bai, H. M. Wu, S. Q. Wang, G. X. Zhang, C. Q. Feng, H. K. Liu, *Appl. Surf. Sci.* **2019**, 488, 512; b) S. Liu, D. Li, G. Zhang, D. Sun, J. Zhou, H. Song, *ACS Appl. Mater. Inter.* **2018**, 10, 34193.

[31] a) Z. Li, S. Xiao, J. Liu, X. Niu, Y. Xiang, T. Li, J. S. Chen, *Acta Metall. Sin-engl.* **2021**, 34, 373; b) Y. Liu, Y. Xu, Y. Han, Z. Zhang, J. Xu, Y. Du, J. Bao, X. Zhou, *J. Power Sources* **2019**, 436, 226860.

[32] M. Ma, S. Zhang, Y. Yao, H. Wang, H. Huang, R. Xu, J. Wang, X. Zhou, W. Yang, Z. Peng, X. Wu, Y. Hou, Y. Yu, *Adv. Mater.* **2020**, 32, 2000958.

[33] a) V. V. Kulish, O. I. Malyi, C. Persson, P. Wu, *Phys. Chem. Chem. Phys.* **2015**, 17, 13921; b) K. Xu, P. Chen, X. Li, Y. Tong, H. Ding, X. Wu, W. Chu, Z. Peng, C. Wu, Y. Xie, *J. Am. Chem. Soc.* **2015**, 137, 4119.

[34] C. Fall, N. Binggeli, A. Baldereschi, *J. Phys.: Condens. Matter* **1999**, 11, 2689.

[35] N. Holmberg, K. Laasonen, P. Peljo, *Phys. Chem. Chem. Phys.* **2016**, 18, 2924.

[36] L. Cheng, Y. Hu, L. Ling, D. Qiao, S. Cui, Z. Jiao, *Electrochim. Acta* **2018**, 283, 664.